RESEARCH REPOSITORY

This is the author's final version of the work, as accepted for publication following peer review but without the publisher's layout or pagination. The definitive version is available at:

Deditius, A.P. and Reich, M. (2016) Constraints on the solid solubility of Hg, Tl, and Cd in arsenian pyrite. American Mineralogist, 101 (6). pp. 1451-1459.

Constraints on the solid solubility of Hg, Tl, and Cd in arsenian pyrite

Artur P. Deditius[1], Martin Reich[2,3]

[1]Murdoch University, School of Engineering and Information Technology, 90 South Street, Murdoch, Western Australia 6150, Australia

[2]Department of Geology, FCFM, Universidad de Chile, Plaza Ercilla 803, Santiago, Chile

[3]Andean Geothermal Center of Excellence, FCFM, Universidad de Chile, Plaza Ercilla 803, Santiago, Chile

Abstract

Arsenic-rich (arsenian) pyrite can contain up to tens of thousands of parts per million (ppm) of toxic heavy metals such as Hg, Tl, and Cd, although few data are available on their solid solubility behavior. When a compilation of Hg, Tl, and Cd analyses from different environments are plotted along with As in a M(Hg, Tl, and Cd)-As log-log space, the resulting wedge-shaped distribution of data points suggests that the solid solubility of the aforementioned metals is strongly dependent on the As concentration of pyrite. The solid solubility limits of Hg in arsenian pyrite—i.e., the upper limit of the wedge-shaped zone in compositional space—are similar to the one previously defined for Au by Reich et al. (2005) ($C_{Hg,Au} = 0.02C_{As} + 4 \times 10^{-5}$), whereas the solubility limit of Tl in arsenian pyrite is approximated by a ratio of Tl/As = 1. In contrast, and despite a wedge-shaped distribution of Cd-As data points for pyrite in Cd-As log-log space, the majority of Cd analyses reflect the presence of mineral particles of Cd-rich sphalerite and/or CdS. Based on these data, we show that arsenian pyrite with M/As ratios above the solubility limit of Hg and Tl contain nanoparticles of HgS, and multimetallic Tl-Hg mineral nanoparticles. These results indicate that the uptake of Hg and Tl in

pyrite is strongly dependent on As contents, as it has been previously documented for metals such as Au and Cu. Cadmium, on the other hand, follows a different behavior and its incorporation into the pyrite structure is most likely limited by the precipitation of Cd-rich nanoparticulate sphalerite. The distribution of metal concentrations below the solubility limit suggests that hydrothermal fluids from which pyrite precipitate are dominantly undersaturated with respect to species of Hg and Tl, favoring the incorporation of these metals into the pyrite structure as solid solution. In contrast, the formation of metallic aggregates of Hg and Tl or mineral nanoparticles in the pyrite matrix occurs when Hg and Tl locally oversaturate with respect to their solid phases at constant temperature. This process can be kinetically enhanced by high-to-medium temperature metamorphism and thermal processing or combustion, which demonstrates a retrograde solubility for these metals in pyrite.

Introduction

Pyrite (FeS_2) is the most common sulfide in the upper crust and can host from a few parts per million (ppm) up to weight percent (wt%) levels of heavy metals and metalloids such as As, Hg, Tl, and Cd (Rickard and Luther 2007; Deditius et al. 2008; Lefticariu et al. 2011; Keith et al. 2016). Mineral processing of gold-bearing arsenian pyrite and combustion of pyrite-bearing coal result in the liberation of these toxic elements into the environment posing significant threats to the biosphere (Ikramuddin et al. 1986; Wang et al. 2010; Kolker 2012). For example, 810 Mt/year of Hg are released into the atmosphere as a result of coal combustion (Pirrone et al. 2010), and industrial processing is responsible for the mobilization of 2000–5000 t/year of Tl (Kazantzis 2000; John Peter and Viraraghavan 2005). Furthermore, recent studies have estimated the emission of 4.7 t/year of Cd from sulfide ore mining and 10 t/year in air from basic non-ferrous metals manufacture in Australia (Kyle et al. 2011). In the particular case of As, there are numerous studies reporting natural and anthropogenic contamination of water and soil, and its effects on human health (Plant et al. 2014). Among the numerous toxicological effects of As and heavy metals (Tl, Hg, and Cd) on biota,

carcinogenic, and brain dysfunction effects are considered some of the most important for human life (Kyle et al. 2011 and references therein).

In arsenian (As-rich) pyrite, previous studies have revealed that Hg and Tl tend to accumulate in zones where precious metals such as Au are concentrated, particularly, in low-temperature (<200 °C) sedimentary environments, Carlin-type, and epithermal Au deposits (Cline 2001; Emsbo et al. 2003; Reich et al. 2005; Barker et al. 2009; Deditius et al. 2011; Large et al. 2014). In contrast, it is known that Cd partitions into sphalerite (ZnS) and/or Cd-sulfides under higher-temperature magmatic-hydrothermal conditions and in submarine hydrothermal vents (Cook et al. 2009; Pass 2010; Lockington et al. 2014; Revan et al. 2014; Keith et al. 2016). Metal incorporation into pyrite is complex and studies have shown that both speciation (structurally bound vs. nanoparticulate) and concentration (ppm to wt% levels) are controlled by the incorporation of As into the structure (Reich et al. 2005; Deditius et al. 2014). For example, transmission electron microscopy (TEM) observations have revealed that metals like Au (and associated Hg) in pyrite are commonly hosted as nanoparticles (NPs) or are incorporated into solid solution, particularly in the As-rich growth bands and sectors (Palenik et al. 2004; Deditius et al. 2011). The coupled geochemical behavior between metals and arsenic (e.g., Au vs. As) is clearly exemplified by the solid solubility model proposed by Reich et al. (2005) for Carlin-type and epithermal Au deposits where the Au content of pyrite is a function of As content. Using micro-analytical (EMPA, SIMS) and spectroscopic analyses (synchrotron XANES), the aforementioned authors showed that when Au-As data points are plotted on an Au vs. As log-log space, an As-dependent Au solubility curve defines two fields where Au is present as native Au nanoparticles (above the solubility curve) or as solid solution Au^{1+} (below the solubility curve). Recently, this solubility limit was extended to all types of ore deposits containing pyrite (Deditius et al. 2014), and recent studies have reported a significant relation between As and metals such as Ag and Cu, to name a few (Reich et al. 2010, 2013).

Despite these advances, to the best to our knowledge, there is no detailed information on the behavior of Hg, Tl, and Cd in pyrite and their potential dependence on the contained As of the pyrite mineral host. In one of the very few studies documenting this particular association, Zhou et al. (2005) report

elevated concentrations of Tl (up to 3.5 wt%) in pyrite from the Xiangquan deposit in China that correlate with high concentrations of As (up to 2.6 wt%) and Hg (up to 400 ppm). In this Tl deposit, thallium occurs mainly in As- and Hg-rich pyrite with minor amounts of lorandite ($TlAsS_2$) and hutchinsonite ($TlFeS_2$), strongly suggesting a complex incorporation of these metals in pyrite. Furthermore, experimental evidence suggests that sorption of Cd and other soft Lewis acids in the natural environment suppresses FeS_2 oxidation and may retard the release of acidity and trace metals to the environment (Bostick et al. 2000). However, the particular role of As during Hg, Tl, and Cd uptake and release remains obscure. This significant gap in understanding of the geochemical behavior of Hg, Tl, and Cd in arsenian pyrite encouraged us to test the hypothesis that these metals have solid solubility behavior in arsenian pyrite that is similar to that of Au.

Coupled geochemistry of Hg, Tl, Cd, and As in pyrite

A compilation of previously published electron microprobe analyzer (EMPA), secondary ion mass spectrometry (SIMS), laser ablation-inductively coupled plasma-mass spectrometry (LA-ICP-MS), proton-induced X-ray emission (PIXE), instrumental neutron activation analysis (INAA) data was used to constrain elemental relations between Hg, Tl, Cd, and As in pyrite (Table 1). Data was compiled for pyrite from various environments including porphyry Cu, epithermal and orogenic Au, volcanogenic massive sulfide (VMS), Witwatersrand and Carlin-type Au deposits, and pyrite-bearing metamorphic rocks, sedimentary sequences and coal beds. This work provides a compilation of pyrite analyses obtained by methods that combine low-detection limits (parts per million levels) such as SIMS, LA-ICP-MS, and PIXE, with high-spatial resolution techniques (EMPA).

Concentrations of Hg, Tl, and Cd in pyrite in these environments vary from below the detection to ~15 000 ppm. With the exception of pyrite from the Mt. Polley porphyry Cu-Ag-Au deposit, more than 99% of the metals' analyses in arsenian pyrite plot below the M/As = 1; where M = Hg, Tl, and Cd (Figs. 1a–1c). In all three cases, the distribution of the data points approximates the wedge-shaped zone interpreted as the solid solubility limit for Au in arsenian pyrite (Reich et al. 2005; Deditius et al.

2014). The highest content of Hg and Tl was measured in pyrite from Carlin-type, epithermal and coal deposits, while the highest concentrations of Cd (up to ~1000 ppm) occur in pyrite from porphyry Cu deposits, VMS deposits, and sedimentary environments (Figs. 1a–1b). No data for Cd is available for pyrite from Carlin-type deposits.

Mercury

Figure 1a displays a positive trend of increasing Hg and As contents in pyrite. The lowest content of Hg, ~0.01–10 ppm, was reported for pyrite from porphyry (Cu-Au-Mo) deposits, sedimentary pyrite, and orogenic Au deposits (Pass 2010; Franchini et al. 2015; Marin-Carbonne et al. 2014; Palenova et al. 2015). In contrast, the highest amounts of Hg were found in pyrite from Carlin-type and epithermal Au deposits (Cline 2001; Emsbo et al. 2003; Deditius et al. 2011). Except for a few outliers, almost all the data plot below the Hg/As = 1 limit (Fig. 1a). As a reference, the As-dependent solubility limit of Au is shown. EMPA data of Hg-rich (500–1900 ppm) arsenian pyrite from the Lone Tree Au deposit in Nevada plot above the solubility limit defined by Reich et al. (2005) ("nanoparticle field," NP), and close to the ratio Hg/As = 1 that marks the upper limit of the datapoint cloud (Fig. 1a, black triangles, circled and labeled "NP"). High-resolution TEM observations of the high-Hg pyrite revealed the presence of HgS nanoparticles (NPs) (Deditius et al. 2011). Therefore, analytical data are indicative of the occurrence of Hg-bearing NPs when Hg and As concentrations exceed the solubility limit in pyrite by Reich et al. (2005), or Hg/As ratios approach unity (Fig. 1a). A similar behavior was observed for Hg-bearing metamorphic pyrite, where Hg partitions into the low-temperature melt (<420 °C, greenschist facies) and recrystallizes as complex Tl-Hg-As-Sb-(Ag,Cu)-Pb sulfosalts in pyrite samples from Alpi Apuane (Biagioni et al. 2013). These analyses also plot above the solubility limit (in the NPs field), close to Hg/As = 1 (Fig. 1a, open squares, circled and labeled "NP").

In contrast, high-Hg and high-As contents of pyrite in the Deep Star Carlin-type deposit in Nevada plot below the solubility defined by Reich et al. (2005), and at Hg/As ratios lower than 1 (Hg: 900–14 300 ppm, As: >50 000 ppm As, Fig. 1a). TEM observations and XANES analyses of these anomalously Hg-As-rich pyrite samples show no evidence of Hg-bearing NPs (Reich et al. 2005).

Therefore, Hg-As data points plotting below the solubility limit are interpreted to contain structurally bound or solid solution Hg (Fig. 1a, oval, labeled "SS").

Our analysis shows, as a first approximation, that the As-dependent solubility limit of Au in Figure 1a is a good proxy to evaluate the speciation of Hg in pyrite, i.e., Hg is incorporated in solid solution at lower Hg/As ratios, while its incorporation is favored as NPs at high-Hg/As ratios. A similar behavior/feature of solid solubility for Hg and Au in pyrite is expected, considering the ability of these two metals to form alloys and amalgams even at the nanoscale (Schopf et al. 2015). However, it is important to mention that this behavior is observed in the higher range of concentrations of As and Hg, i.e., >1000 ppm and >100 ppm, respectively (Fig. 1a). Unfortunately, no nano-analytical and spectroscopic information of Hg and As in pyrite is available for samples characterized by lower amounts of these elements (i.e., <100 ppm for both Hg and As).

Thallium

Figure 1b shows that Tl-As data of pyrite from different environments form a similar wedge-shaped zone, limited above by a line of approximate slope Tl/As = 1. Pyrite from Carlin-type and coal deposits contain the highest amount of Tl, while the concentrations of Tl in pyrite from porphyry Cu and orogenic Au deposits are generally below 1 ppm. This can be attributed to the volatile nature of Tl and its strong affinity toward organic matter. A recent review of the composition of sedimentary pyrite by Large et al. (2014) revealed a broad range of Tl concentrations varying from 0.1–10 000 ppm. The majority of these analyses plot below a Tl/As ratio of 1 (Fig. 1b). Similarly to Hg, Tl-bearing NPs in pyrite were observed in metamorphic settings, suggesting that metamorphism induced the mobilization of multimetallic melts (Biagioni et al. 2013). These representative Tl-As analyses plot homogenously above the indicated Tl/As = 1, over range of As concentrations from tens to ten-thousands of parts per million. Unfortunately, there is no nanostructural or spectroscopic data that would help constrain the speciation and/or its structural position of Tl in arsenian pyrite. However, Kouzmanov et al. (2010) did not notice any Tl particles (or other metallic nanonuggets) during LA-ICP-MS profiling of pyrite from the Rosia Poeni porphyry Cu deposit. Therefore, acknowledging the fact that it is not straightforward to establish precise Tl-As solubility relations with the available data,

we suggest that the upper limit ratio Tl/As = 1 may represent, as a first approximation, the solid solubility limit of Tl in arsenian pyrite (i.e., analyses plotting below Tl/As ratios of 1 represent Tl in solid solution, while data points plotting above this limit are most likely related to the presence of Tl-bearing nanoinclusions).

Cadmium

Similarly to Hg and Tl, the majority of Cd data points cluster in a wedge-shaped zone and plot below the M/As ratio of 1 (Fig. 1c). The amount of Cd in pyrite varies significantly between the different types of ore deposits. The highest contents of Cd, >5 ppm, have been reported for pyrite from porphyry Cu deposits, hydrothermal vents in mid-ocean ridges, and volcanic precipitates (Yudovskaya et al. 2006; Pass 2010; Revan et al. 2014; Keith et al. 2016), while the lowest amounts (below parts per million levels) have been found in As-poor pyrite from epithermal Au deposits (Franchini et al. 2015) (Fig. 1b). Most of the data points come from sedimentary settings, where variable Cd concentrations spread from parts per billion up to thousands of parts per million levels (Large et al. 2014) (Fig. 1c). Unfortunately, there is no data available to constraint the structural behavior of Cd in arsenian pyrite or predict the presence of Cd NPs vs. solid solution incorporation. However, it has been suggested that Cd partitions into sulfide nano- and/or micro-particles and crystallizes as CdS and/or Cd-rich sphalerite in pyrite under wide range of temperatures (from 250–650 °C) conditions (Hannington et al. 1988, 1991; Genna and Gaboury 2015; Keith et al. 2016).

Therefore, it is likely that higher concentrations of Cd contents in pyrite from porphyry Cu deposits, hydrothermal vents (VMS) and volcanic precipitates (Fig. 1c) represent inclusions of Cd-sulfides and or sphalerite, as previously reported (Hannington et al. 1988, 1991; Genna and Gaboury 2015; Keith et al. 2016). The data points representing Cd in sphalerite NPs plot in the field of nanoparticles and solid solution, Thus, it is likely the wedge-shaped distribution of the Cd data points in the Cd-As log-log space below the Cd/As = 1 ratio does not indicate a solubility limit, despite its position to be similar to the one for Au, Hg, and Tl (Fig. 1c).

Intrinsic controls on the solubility limit of Hg, Tl, and Cd in arsenian pyrite

Our compilation and review of the available data on the behavior of Hg, Tl, and Cd in arsenian pyrite has revealed the presence of similar compositional features previously reported for Au (e.g., Reich et al. 2005; Deditius et al. 2014). Perhaps the most noticeable first-order feature observed is the wedge-shaped pattern that arises when Hg, Cd, and Tl concentrations are plotted against As. These wedge-shaped zones are limited above by a solubility limit in compositional log-log space, which can be approximated either by the solubility relation found for Au by Reich et al. (2005) (for Hg, Cd, and Au: $C_{Hg,Cd,Au} = 0.02C_{As} + 4 \times 10^{-5}$, see curve in Fig. 1) or, for the particular case of Tl, by a Tl/As ratio of ~1 (Fig. 1b). While these relationships suggest some common and fundamental mechanisms controlling the uptake as Au, Hg, and Tl into arsenian pyrite, the behavior of Cd seem to be controlled by the precipitation of mineral nanoparticles of sphalerite and/or Cd-sulfides and is more likely related to fluid-mineral interaction. The described features are relevant to explore the mechanisms of incorporation of Hg, Tl, and Cd into pyrite, but may also have a similar impact when evaluating the release of such metals from the arsenian pyrite matrix.

It has been documented that the incorporation of anionic (As^{1-}, Simon et al. 1999; Abraitis et al. 2004) or cationic (As^{3+}, Deditius et al. 2008) arsenic species into the pyrite structure facilitates substitution of other metals, most noticeable Au. Similar behavior reported here for the heavy metals Hg and Tl in arsenian pyrite may be related to the relatively small differences in their crystal radii with respect to Au. Substitutional mechanisms discussions are commonly limited to the formal charges, which should be treated with caution considering the covalent type of bonding in sulfides, i.e., Au^+ and Au^{3+} (0.157 and 0.099 nm, respectively), Hg^+ and Hg^{2+} (0.133 and 0.116 nm, respectively), Tl^+ and Tl^{3+} (0.164 and 0.1025 nm, respectively), (data after Shannon 1976, for octahedral coordination).

The incorporation of Hg and Tl depends on the presence of other substitutions in the pyrite structure. Therefore, changes in the semi-conducting behavior of pyrite surfaces during crystal growth may have a significant impact on metal uptake, i.e., As and Sb promote *p*-type conductivity, while the presence of divalent metals such as Co and/or Ni in the structure induces *n*-type conductivity (Pearce et al.

2006 and references therein). Substitution of As for S in the tetrahedral position generates a hole in the Fe *d*-like valence band, which makes As an acceptor capable of accommodating one electron from the valence band, and as a consequence, a charge carrier. Such contrasting As vs. Co/Ni-rich areas may occur within a single crystal of pyrite. In addition, the increase in As contents in pyrite expands the unit cell and creates structural distortion. Therefore, a combination of the electrical and crystal-chemical properties of As may generate favorable conditions promoting the incorporation of heavy metals in pyrite in natural environments (Lehner et al. 2006, 2012). In the case of synthetic materials, it has been reported that *p*-type conductivity promotes high-solid solubility of Au in semiconductors matrices such as silicon (O'Shaughnessy et al. 1974). Because *p*-type conductivity occurs in phosphorous-doped synthetic pyrite (Blenk et al. 1993), it is very likely that the effects on metal behavior are similar. In particular, phosphorous-bearing pyrite crystals have complex morphologies such as combinations of {111}, {110}, and {100} forms that have also been observed in natural As and Au-rich hydrothermal pyrites (Chouinard et al. 2005). However, the influence of As on pyrite morphology remains ambiguous, as some authors report enhanced development of the {111} face (Sunagawa and Takahashi 1955), while others document higher contents of As in |*hk*0| sectors (Chouinard et al. 2005).

The other important factor that may regulate the amount of impurities in the pyrite structure is the size of the single crystals, which can be as small as 8 nm (Deditius et al. 2008). Material science provides evidence for nanoparticulate semiconductors that experience self-purification resulting in the expulsion of the non-stoichiometric impurities/dopants toward the grain boundaries (Erwin et al. 2005 and references therein). This feature is consistent with the occurrence of "invisible" (i.e., refractory) Tl in hydrothermal coarse-grained pyrite from Xiangquan thallium deposit (China), which contains up to 35 000 ppm. In contrast, the amounts of Tl, Hg, and Cd in the colloidal form of pyrite in this deposit were below 9300, 400, and 230 ppm, respectively (Zhou et al. 2005). Such behavior is mainly controlled by the surface morphology, shape of the nanocrystals, and surfactants in the solution. While in synthetic systems the diffusion of the trace element (Mn) in semiconductors (CdSe) around temperature of 300 °C is negligible, 1–3 Å in short time (1 h) (Jamil and Shaw 1994), the

equilibration and homogeneous distribution of the trace element within individual nanoparticles can be achieved over the geological time scale (Reich et al. 2006; Deditius et al. 2008; González-Jiménez et al. 2015). Moreover, it was found that the formation of trace element-rich semiconducting NPs—with homogeneously distributed doping element—is possible when the trace element is adsorbed on the growing surface of the nanocrystal (Erwin et al. 2005). Consequently, the rate of kinetically controlled growth of pyrite must exceed the rate of equilibration and removal of the impurities to accommodate Au, Hg, and Tl in the crystal structure. This kinetically controlled formation of pyrite under lower temperature conditions (e.g., collomorphic pyrite, Huston et al. 1995; Abraitis et al. 2004), promotes distortion of the pyrite structure and incorporation of higher quantities of large metals. This is envisaged by a positive correlation between Tl (up to about 8000 ppm) and As in porous pyrite associated with the (As,Sb)-growth zones, which have been interpreted to be a result of precipitation from hydrothermal fluids originating from multiple sources (Ingham et al. 2014). It is likely that the presence of As-promoting distortion and surface modification enables incorporation of the large cations, Au, Hg, and Tl, via stoichiometric or nonstoichiometric substitutions involving the formation of vacancies (Chouinard et al. 2005; Deditius et al. 2008), or nanoscale phase decomposition such as polycrystalline pyrite nano-aggregates (Palenik et al. 2004).

Role of fluid composition and temperature

First, the chemical composition of the fluid is one of the main factors that control metal uptake during pyrite growth. For example, the presence of Hg-rich growth zoning on pyrite in Carlin-type and epithermal Au deposits is indicative that the deposition of Hg is restricted by its availability in the fluid, similar to Au (Barker et al. 2009). In sedimentary environments, pyrite is a natural sink for Hg during coal formation, where recrystallized pyrite can incorporate up to 7600 ppb of Hg (Hannington et al. 1991; Lefticariu et al. 2011). In both examples, the mechanism of Hg incorporation would involve the breakdown of aqueous Hg complexes and the adsorption of Hg species onto the growing pyrite surfaces. It is likely that this process is enhanced by local fluid oxidation (Chouinard et al. 2005; Barker et al. 2009) and the presence of As in the mineralizing fluid (see previous section).

Chemisorption of metal species onto pyrite surfaces can result in a highly efficient mechanism for sequestering metals from mineralizing fluids. Ehrhardt et al. (2000) reported partial oxidation of pyrite surfaces during adsorption of Hg^{2+} with the formation of inner surface complexes. This mechanism is supported by XPS and XAS studies of Hg incorporation into pyrite, which revealed formation of surface complexes between S(-I) and Hg(II) (Behra et al. 2001), and Hg-Cl complexes on the pyrite surface (Bower et al. 2008). No native Hg or Hg-sulfides were found in these studies. Unlike Hg (or Tl), the relatively small amounts of Cd present in pyrite may be a result of the decreasing efficiency of Cd uptake with increasing concentration in the pyrite surface (Parkman et al. 1999). The lack of separation between the data points representing nanoparticulate Cd-rich sphalerite and Cd in solid solution in pyrite (Fig. 1c) suggests that Cd incorporation into pyrite is not controlled by solid-state solubility rules. In contrast, it is suggested that sphalerite NPs form at the pyrite-fluid interface due to rapid precipitation from the Cl-depleted fluids, which become supersaturated with respect to (Zn,Cd)-sulfides (Reich et al. 2013; Keith et al. 2016). In addition, Bostick et al. (2000) proposed reconstruction and disproportionation of pyrite surface that resulted in the mixture of native sulfur, Fe-hydroxides and CdS, supporting preferential formation of particulate sulfides rather than incorporation into the structure as solid solution (Fig. 1c).

Second, the temperature of pyrite formation or subsequent metamorphism is a key factor controlling the metal budget of pyrite in geologic environments. The identification of particulate Hg and Tl in pyrite in low-temperature metamorphic rocks by Biagioni et al. (2013) demonstrates that low-temperature recrystallization processes involving trace element-rich pyrite are one of the most important factors controlling the post-entrapment mobilization of these metals (Fig. 1). The temperature of mobilization depends on the association of metals; i.e., the larger the numbers of metals, characterized by low-temperature melting, chemically connected in the structure of the hosting sulfide the lower the melting temperature of the sulfide domain (Tomkins et al. 2007); the melting temperatures of Tl-Au, Hg-Au, and Bi-Au systems are as low as 147, 39, and 241 °C, respectively (Okamoto and Massalski 1987).

The in situ thermal stability experiments by Reich et al. (2006) are one of the very few studies that document the effect of temperature on metal nanoparticle stability in pyrite. In this study, native Au NPs of ~10 nm begin to dissolve in the As-rich pyrite matrix and diffusively growth at the expense of smaller ones at temperatures close to 400 °C. Therefore, it is likely that Hg, Tl, and Cd may be liberated much easier from the structure of a distorted, nanoparticulate, As-rich pyrite matrix. However, it is expected that these metals will behave differently within multimetallic NPs with the increase of temperature as envisaged by separation of Pt and Au, diffusion of Au through the Ag_2S, and its Ostwald ripening-based recrystallization on the surface of Ag_2S (Yang and Ying 2010). Alternatively, the aggregates of separate mineral NPs will form alloys with the temperature increase (Bonifacio et al. 2015). For example, given the paucity of information on the occurrence of Tl NPs in well-investigated pyrite samples suggests that Tl preferentially dissolves into the pyrite matrix (see Fig. 1b), rather than forming separate domains of Tl-sulfides. This might be related to the possible higher oxidation state of Tl^{3+} in collomorphic pyrite (Huston et al. 1995). In addition, the decrease in the Fe content in pyrite will promote formation of "liquid-like" As-Fe-S NPs entrapped in the arsenian pyrite structure (Deditius et al. 2009), which in turn may sequester migrating/diffusing metals. The separation of metallic nanodomains is also supported by positive correlation between Cd and Zn in pyrite from paleo-chimneys, which suggests that Cd is incorporated by micro-inclusions of sphalerite (Revan et al. 2014; Genna and Gaboury 2015; Keith et al. 2016). In addition, under hydrothermal conditions >344 °C HgS (metacinnabar) precipitates from Hg^{2+}-aqueous solutions rich in S(-II), while cinnabar is forming below the indicated temperature (Barnes and Seward 1997).

Consequently, the behavior of Hg, Tl, and Cd in arsenian pyrite is an outcome of primary intrinsic factors, in the studied case, the presence of As-rich pyrite surface and extrinsic features of the environment in which pyrite forms. These include: (1) "fluid"-control, i.e., chemical composition of the hydrothermal fluid; which also impacts the surface morphology and thus controls chemisorption and processes of "solid solution" incorporation, and (2) a temperature control that influences stability of the matrix, formation and stability of NPs.

Geochemical implications and future studies

Based on the aforementioned discussion, we propose a conceptual model that describes the behavior of Hg, Tl, and Au in the metal-As-*T* space (Fig. 2). Figure 2 shows that the two fields NPs and solid solution are separated by bowl-like solubility surface with the crest of solubility limit after Reich et al. (2005) projected from the As-Au space. Note that this solubility limit crest may shift up- and downward along the solubility plane with the changes in the temperature (Fig. 2). The increase in temperature is likely to cause metal mobilization from pyrite during recrystallization and high-temperature alteration under metamorphic conditions reported for orogenic Au deposits (Sung et al. 2009). On the contrary, cooling will promote formation of metallic mineral NPs in case of As-poor pyrite across all geological environments as discussed in detail by Deditius et al. (2014).

The recognition of solid solubility limits for Hg and Tl, and the presence of micro-to-nanoparticulate Cd in pyrite, provide new insights into the environmental sequestration of Hg, Tl, and Cd. Until now, the geochemical behavior of Hg and Tl in pyrite was exclusively linked with the presence mineral particles and/or (non)stoichiometric structural substitutions. We suggest that the uptake of Hg and Tl into arsenian pyrite is strongly tied to presence of As, and that the occurrence of these metals as nanoparticles vs. solid solution in pyrite may be predicted if the solid solubility limits are precisely determined using a combination of experimental, analytical, and spectroscopic data. The distribution of most of the analyses below the solubility limit suggests that Hg and Tl are preferentially incorporated as structurally bound species in pyrite, probably through chemisorption processes in aqueous solutions that are mostly undersaturated with respect to their native metals species or mineral NPs (Figs. 1 and 2). Furthermore, the restricted occurrence of Hg and Tl nanoparticles in arsenian pyrite, as predicted by the solid solubility limits, is most likely the result of local oversaturation of aqueous solutions and/or post-entrapment modifications resulting from changes in temperature during diagenesis or metamorphism. The documented lack of a solubility limit for Cd in arsenian pyrite can be extended to other elements, e.g., Pb, Ag, Te, and Sb, which have been detected in significant concentrations in pyrite but predominantly occur as micro-to-nanoscale inclusions in porous zones (Pačevski et al. 2012).

Considering the scarce nanostructural and largely non-systematic information available for hazardous metals in pyrite, future studies aiming to elucidate the geochemical cycle of these elements should incorporate a combination of experimental approach and studies of representative natural samples involving: (1) determination of the major and trace element composition using a combination of EMPA, SIMS, and/or LA-ICP-MS; (2) preliminary tests to target NPs (e.g., FE-SEM observations, and depth profiling using SIMS or LA-ICP-MS); (3) sampling prospective areas of pyrite using focused-ion beam (FIB); (4) TEM studies to detect, image, and resolve the crystal-chemistry of NPs; and (5) synchrotron-based XANES and EXAFS studies to determine the oxidation state and/or speciation of trace elements.

References cited

Abraitis, P.K., Pattrick, R.A.D., and Vaughan, D.J. (2004) Variations in compositional, textural and electrical properties of natural pyrite: a review. International Journal of Mineral Processing, 74, 41–59.

Agangi, A., Hofman, A., and Wohlgemuth-Ueberwasser, C.C. (2013) Pyrite zoning as a record of mineralization in the Ventersdorp contact reef, Witwatersrand Basin, South Africa. Economic Geology, 108, 1243–1272.

Barker, S.L.L., Hickey, K.A., Cline, J.S., Dipple, G.M., Kilburn, M.R., Vaughan, J.R., and Longo, A.A. (2009) Uncloaking invisible gold: Use of nano-SIMS to evaluate gold, trace elements, and sulphur isotopes in pyrite from Carlin-type gold deposits. Economic Geology, 104, 897–904.

Barnes, H.L., and Seward, T.M. (1997) Geothermal systems and mercury deposits. In H.L. Barnes, Ed., Geochemistry of Hydrothermal Ore Deposits, 3rd ed., p. 699–736. Wiley, New York.

Behra, P., Bonnissel-Gissinger, P., Alnot, M., Revel, R., and Erhardt, J.J. (2001) XPS and XAS study of the sorption of Hg(II) onto pyrite. Langmuir, 17, 3970–3979.

Berner, Z.A., Puchelt, H., Nöltner, T., and Kramaer, U. (2013) Pyrite geochemistry in the Taoracian Posidonia Shale of south-west Germany: Evidence for contrasting trace-element patterns of diagenetic and syngenetic pyrites. Sedimentology, 60, 548–573.

Biagioni, C., D'Orazio, M., Vezzoni, S., Dini, A., and Orlandi, P. (2013) Mobilization of Tl-Hg-As-Sb-(Ag,Cu)-Pb sulfosalt melts during low-grade metamorphism in the Alpi Apuane (Toscany, Italy). Geology, 41, 747–750.

Blenk, O., Bucher, E., and Willeke, G. (1993) *p*-type conduction in pyrite single crystals prepared by chemical vapor transport. Applied Physics Letters, 62, 2093.

Bonifacio, C.S., Carenco, S., Wu, C.-H., House, S.D., Bluhm, H., and Yang, J.C. (2015) Thermal stability of core-shell nanoparticles: A combined in situ study by XPS and TEM. Chemistry of Materials, 27, 6960–6968.

Bostick, B.C., Fendorf, S., and Fendorf, M. (2000) disulphide disproportionation and CdS formation upon cadmium sorption on FeS2. Geochimica et Cosmochimica Acta, 64, 247–255.

Bower, J., Savage, K.S., Weinman, B., Barnett, M.O., Hamilton, W.P., and Harper, W.F. (2008) Immobilization of mercury by pyrite (FeS2). Environmental Pollution, 156, 504–514.

Cabral, A.R., Koglin, N., Strauss, H., Brätz, H., and Kwitko-Ribero, R. (2013) Regional sulphate-hematite-sulfide zoning in the auriferous Mariana anticline, Quadrilétero Ferrífero of Minas Gerais, Brazil. Mineralium Deposita, 48, 805–816.

Cepedal, A., Fuertes-Fuente, M., Martin-Izard, A., González-Instal, S., and Barrero, M. (2008) Gold-bearing As-rich pyrite and arsenopyrite from the El Valle gold deposit, Asturias, northwestern Spain. Canadian Mineralogist, 46, 233–247.

Chouinard, A., Paquette, J., and Williams-Jones, A.E. (2005) Crystallographic controls on trace-element incorporation in auriferous pyrite from the Pascua epithermal high-sulfidation deposit, Chile-Argentina. Canadian Mineralogist, 43, 951–963.

Cline, J.S. (2001) Timing of gold and arsenic sulfide mineral deposition at the Getchell Carlin-type gold deposit, North-Central Nevada. Economic Geology, 96, 75–89.

Cook, N.J., Ciobanu, C.L., Pring, A., Skinner, W., Shimizu, M., Danyushevsky, L., Saini-Eidukat, B., and Melcher, F. (2009) Trace and minor elements in sphalerite: A LA-ICP-MS study. Geochimica et Cosmochimica Acta, 73, 4761–4791.

Deditius, A.P., Utsunomiya, S., Renock, D., Ewing, R.C., Ramana, C.V., Becker, U., and Kesler, S.E. (2008) A proposed new type of arsenian pyrite: Composition, nanostructure and geological significance. Geochimica et Cosmochimica Acta, 72, 2919–2933.

Deditius, A.P., Utsunomiya, S., Ewing, R.C., and Kesler, S.E. (2009) Nanoscale "liquid" inclusions of As-Fe-S in arsenian pyrite. American Mineralogist, 94, 391–394.

Deditius, A.P., Utsunomiya, S., Kesler, S.E., Reich, M., and Ewing, R.C. (2011) Trace elements nanoparticles in pyrite. Ore Geology Reviews, 42, 32–46.

Deditius, A.P., Reich, M., Kesler, S.E., Utsunomiya, S., Chryssoulis, S.L., Walshe, J., and Ewing, R.C. (2014) The coupled geochemistry of Au and As in pyrite from hydrothermal ore deposits. Geochimica et Cosmochimica Acta, 140, 644–670.

Deol, S., Deb, M., Large, R.R., and Gilbert, S. (2012) LA-ICPMS and EMPA studies of pyrite, arsenopyrite and loellingite from the Bhukia-Jagpura gold prospect, southern Rajastan, India: Implicaitons for ore genesis and gold remobilization. Chemical Geology, 326-327, 72–87.

Ding, Z., Zheng, B., Long, J., Belkin, H.E., Finkelman, R.B., Chen, C., Zhou, D., and Zhou, Y. (2001) Geological and geochemical characteristics of high arsenic coals from endemic arsenosis areas in southwestern Guizhou Province, China. Applied Geochemistry, 16, 1353–1360.

Duchesne, J.C., Rouhart, A., Schoumacher, C., and Dillen, H. (1983) Thallium, nickel, cobalt and other trace elements in iron sulphides from Belgian lead-zinc vein deposits. Mineralium Deposita, 18, 303–313.

Ehrhardt, J.J., Behra, P., Bonnisel-Gissinger, P., and Alnot, M. (2000) XPS study of the sorption of Hg(II) onto pyrite FeS2. Surface and Interface Analysis, 30, 269–272. Emsbo, P., Hofstra, A.H., Lauha, E.A., Griffin, G.L., and Hutchinson, R.W. (2003) Origin of high-grade gold ore, source of ore fluid components, and genesis of the Miekle and neighbouring Carlin-type deposits, Northern Carlin Trend, Nevada. Economic Geology, 98, 1069–1105.

Erwin, S.C., Zu, L., Haftel, M.I., Efros, A.L., Kennedy, T.A., and Norris, D.J. (2005) Doping semiconductor nanocrystals. Nature, 436, 91–94.

Franchini, M., McFarlane, C., Maydagán, L., Reich, M., Lentz, D.R., Mainert, L., and Bouhier, V. (2015) Trace metals in pyrite and marcasite from the Agua Rica porphyry-high sulfidation epithermal deposit, Catamarca, Argentina: Textural features and metal zoning at the porphyry to epithermal transition. Ore Geology Reviews, 66, 366–387.

Genna, D., and Gaboury, D. (2015) Deciphering the hydrothermal evolution of a VMS system by LA-ICP-MS using trace elements in pyrite: An example from the Bracemac-McLeod deposits, Abitibi, Canada, and implications for exploration. Economic Geology, 110, 2087–2108.

González-Jiménez, J., Reich, M., Camprubí, A., Gervilla, F., Griffin, W.L., Colás, V., O'Reilly, S.Y., Proenza, J.A., Martini, M., Pearson, N.J., and Centeno-García, E. (2015) Thermal metamorphism of mantle chromites and the stability of noble-metal nanoparticles. Contributions to Mineralogy and Petrology, 170, 15.

Griffin, W.L., Ashley, P.M., Ryan, C.G., Sie, S.H., and Suter, G.F. (1991) Pyrite geochemistry in the North Arm epithermal Ag-Au deposit, Queensland, Australia: A proton-microprobe study. Canadian Mineralogist, 29, 185–198.

Hannington, M.D., Thompson, G., Rona, P.A., and Scott, S.D. (1988) Gold and native copper in supergene sulfides from the Mid-Atlantic Ridge. Nature, 333, 64–66.

Hannington, M., Herzig, P., Scott, S., Thompson, G., and Rona, P. (1991) Comparative mineralogy and geochemistry of gold-bearing sulfide deposits on the mid-ocean ridges. Marine Geology, 101, 217–248.

Hofmann, A., Bekker, A., Rouxel, O., Rumble, D., and Master, S. (2009) Multiple sulfur and iron isotope composition of detrital pyrite in Archean sedimentary rocks: A new tool for provenance analysis. Earth and Planetary Science Letters, 286, 436–445.

Hower, J.C., Campbell, J.L., Teesdale, W.J., Nejedny, Z., and Robertson, J.D. (2008) Scanning probe microprobe analysis of mercury and other trace elements in Fesulfides from a Kentucky coal. International Journal of Coal Geology, 75, 88–92.

Huston, D.L., Sie, S.H., Suter, G.F., Cooke, D.R., and Both, R.A. (1995) Trace elements in sulphide minerals from eastern Australian volcanic-hosted massive sulphide deposits: Part I. Proton microprobe analyses of pyrite, chalcopyrite, and sphalerite, and Part II. Selenium levels in pyrite: Comparison with 34S values and implications for the source of sulphur in volcanogenic hydrothermal systems. Economic Geology, 90, 1167–1196.

Ikramuddin, M., Besse, L., and Nordstrom, P.M. (1986) Thallium in the Carlin-type gold deposit. Applied Geochemistry, 1, 493–502.

Ingham, E.S., Cook, N.J., Cliff, J., Ciobanu, C.L., and Huddleston, A. (2014) A combined chemical isotopic and microstructural study of pyrite from roll-front uranium deposits, Lake Eyre Basin, South Australia. Geochimica et Cosmochimica Acta, 125, 440–465.

Jamil, N.Y., and Shaw, D. (1994) The diffusion of Mn in CdSe. Semiconductor Science and Technology, 10, 952–958.

John Peter, A.L., and Viraraghavan, T. (2005) Thallium: a review of public health and environmental concerns. Environment International, 31, 493–501.

Kazantzis, G. (2000) Thallium in the environment and health effects. Environmental Geochemistry and Health, 22, 275–280.

Keith, M., Häckel, F., Haase, K.M., Schwartz-Schampera, U., and Klemd, R. (2016) Trace element systematics of pyrite from submarine hydrothermal vents. Ore Geology Reviews, 72, 728–745.

Kolker, A. (2012) Minor element distribution in iron disulfides in coal: A geochemical review. International Journal of Coal Geology, 74, 32–43.

Kouzmanov, K., Pettke, T., and Heinrich, C.A. (2010) Direct analysis of ore-precipitating fluids: Combined IR microscopy and LA-ICP-MS study of fluid inclusions in opaque ore minerals. Economic Geology, 105, 351–373.

Kyle, J.H., Breuer, P.L., Bunney, K.G., Pleysier, R., and May, P.M. (2011) Review of trace toxic elements (Pb, Cd, Hg, As, Sb, Bi, Se, Te) and their deportment in gold processing. Part 1: Mineralogy, aqueous chemistry and toxicity. Hydrometallurgy, 107, 91–100.

Large, R.R., Maslennikov, V.V., Robert, F., Danyushevsky, L., and Chang, Z. (2007) Multistage sedimentary and metamorphic origin of pyrite and gold in the giant Sukhoi Log deposit, Lena gold province, Russia. Economic Geology, 102, 1233–1267.

Large, R.R., Danyushevsky, L., Hollit, C., Maslennikov, V.V., Meffre, S., Gilbert, S., Bull, S., Scott, R., Emsbo, P., Thomas, H., Singh, B., and Foster, J. (2009) Gold and trace elements zonation in pyrite using laser imaging technique: Implications for the timing of gold in orogenic and Carlin-style sediment-hosted deposits. Economic Geology, 104, 635–668.

Large, R.R., Halpin, J.A., Danyushevsky, L.V., Maslennikov, V.V., Bull, S.W., Long, J.A., Gregory, D.D., Lounejeva, E., Lyons, T.W., Sack, P.J., McGoldrick, P.J., and Calver, C.R. (2014) Trace element content of sedimentary pyrite as a new proxy for deep-time ocean-atmosphere evolution. Earth and Planetary Science Letters, 389, 209–220.

Lefticariu, L., Blum, J.D., and Gleason, J.D. (2011) Mercury isotopic evidence for multiple mercury sources in coal from the Illinois Basin. Environmental Science and Technology, 45, 1724–1729.

Lehner, S.W., Savage, K., and Ayers, J.C. (2006) Vapour growth and characterization of pyrite (FeS2) doped with Ni, Co, and As: Variations in semiconducting properties. Journal of Crystal Growth, 286, 306–317.

Lehner, S.W., Newman, N., van Schilfgaarde, M., Bandyopadhyay, S., Savage, K., and Buseck, P. (2012) Defect energy levels and electronic behaviour of Ni-, Co-, and As-doped synthetic pyrite (FeS2). Journal of Applied Physics, 111, 083717.

Li, N., Deng, J., Yang, L.-Q., Goldfarb, R.J., Zhang, C., Marsh, E., Lei, S.-B., Koenig, A., and Lowers, H. (2014) Paragenesis and geochemistry of ore minerals in the epizonal gold deposits of the Yangshan gold belt, West Qinling, China. Mineralium Deposita, 49, 427–449.

Lockington, J.A., Cook, N.J., and Ciobanu, C.L. (2014) Trace and minor elements in sphalerite from metamorphosed sulphide deposits. Mineralogy and Petrology, 108, 873–890.

Marin-Carbonne, J., Rollion-Bard, C., Bekker, A., Rouxexl, O., Agangi, A., Cavalazzi, B., Wohlgemuth-Ueberwasser, C.C., Hofmann, A., and McKeegan, K.D. (2014) Coupled Fe and S isotope variations in pyrite nodules from Archean shale. Earth and Planetary Science Letters, 392, 67–79.

Okamoto, H., and Massalski, T.B. (1987) Phase Diagrams of Binary Gold Alloys. ASM International, Ohio.

Okrusch, M., Lorenz, J.A., and Weyer, S. (2007) The genesis of sulphide assemblages in the former Wilhelmine mine, Spassart, Bavaria, Germany. Canadian Mineralogist, 45, 723–750.

O'Shaughnessy, T.A., Barber, H.D., Thompson, D.A., and Heasell, E.L. (1974) The solid solubility of gold in doped silicon by oxide encapsulation. Journal of Electrochemical Society, 121, 1350–1354.

Pačevski, A., Moritz, R., Kouzmanov, K., Marquart, K., Živković, P., and Cvetković, L. (2012) Texture and composition of Pb-bearing pyrite from the Čoka Marin polymetallic deposit, Serbia, controlled by nanoscale inclusions. Canadian Mineralogist, 50, 1–20.

Palenik, C.S., Ustunomiya, S., Reich, M., Kesler, S.E., Wang, L., and Ewing, R.C. (2004) "Invisible" gold revealed: Direct imagining of gold nanoparticles in a Carlin-type deposit. American Mineralogist, 89, 1359–1366.

Palenova, E.E., Belogub, E.F., Plotinskaya, O.Yu., Novoselov, K.A., Maslennikov, V.V., Kotlyarov, V.A., Blinov, I.A., Kuzmenko, A.A., and Griboyedova, I.G. (2015) Chemical evolution of pyrite at the Kopylovsky and Kavkaz Black shale-hosted gold deposits, Bodaybo District, Russia: Evidence from EMPA and LA-ICP-MS data. Geology of Ore Deposits, 57, 64–84.

Parkman, R.H., Charnock, J.M., Bryan, N.D., Livens, F.R., and Vaughan, D.J. (1999) Reactions of copper and cadmium ions in aqueous solution with goethite, lepidocrocite, mackinawite, and pyrite. Americam Mineralogist, 84, 407–419.

Pass, H.E. (2010) Breccia-hosted chemical and mineralogical zonation patterns of the northest zone, Mt. Polley Cu-Ag-Au alkali porphyry deposit, British Columbia, Canada. Ph.D. thesis, University of Tasmania, Australia.

Pearce, C.I., Pattrick, R.A.D., and Vaughan, D.J. (2006) Electrical and magnetic properties of sulphides. Review in Mineralogy and Geochemistry, 61, 127–180.

Pirrone, N., Cinnirella, S., Feng, X., Finkelman, R.B., Friedli, H.R., Leaner, J., Mason, R., Mukherjee, A.B., Stracher, G.B., Streets, D.G., and Telner, K. (2010) Global mercury emissions to the atmosphere from anthropogenic and natural resources. Atmospheric Chemistry and Physics, 10, 5951–5964.

Plant, J.A., Bone, J., Voulvoulis, N., Kinniburgh, D.G., Smedley, P.L., Fordyce, F.M., and Klinck, B. (2014) Arsenic and selenium. In H.D. Holland and K.K. Turekain, Eds., Environmental Geochemistry, Treatise on Geochemistry, 11, p. 13–57. Elsevier, Amsterdam.

Reich, M., Utsunomiya, S., Kesler, S.E., Wang, L.M., Ewing, R.C., and Becker, U. (2006) Thermal behaviour of metal nanoparticles in geologic materials. Geology, 34, 1033–1036.

Reich, M., Kesler, S.E., Utsunomiya, S., Palenik, C.S., Chryssoulis, S.L., and Ewing, R.C. (2005) Solubility of gold in arsenian pyrite. Geochimica et Cosmochimica Acta, 69, 2781–2796.

Reich, M., Palacios, C., Chryssoulis, S., Weldt, M., Alvear, M., and Deditius, A. (2010) "Invisible" silver and gold in supergene chalcocite. Geochimica et Cosmochimica Acta, 74, 6157–6173.

Reich, M., Deditius, A.P., Chryssoulis, S., Li, J.W., Ma, C.Q., Parada, M.A., Barra, F., and Mittermayr, F. (2013) Pyrite as a record of hydrothermal fluid evolution in a porphyry copper system: A SIMS/EMPA trace element study. Geochimica et Cosmochimica Acta, 104, 42–62.

Revan, M.K., Genc, Y., Maslennikov, V.V., Maslennikova, S.P., Large, R.R., and Danyushevsky, L.V. (2014) Mineralogy and trace-element geochemistry of sulphide minerals in hydrothermal chimneys from the

Upper-Cretaceous BMS deposits of the eastern Pontide orogenic belt (NE Turkey). Ore Geology Reviews, 63, 129–149.

Rickard, D., and Luther, G.W. III (2007) Chemistry of iron sulphides. Chemistry Reviews, 107, 514–562.

Schackelton, J.M., Spry, P.G., and Bateman, R. (2003) Telluride mineralogy of the Golden Mile deposit Kalgoorlie, Western Australia. Canadian Mineralogist, 41, 1503–1524.

Scher, S., Williams-Jones, A.E., and Williams-Jones, G. (2013) Fumarolic activity, acid-sulfate alteration, and high-sulfidation epithermal precious metal mineralization in the crater of Kawah Ijen volcano, Java, Indonesia. Economic Geology, 108, 1099–1118.

Schopf, C., Martin, A., Schmidt, M., and Lacopino, D. (2015) Investigation of Au-Hg amalgam formation on substrate-immobilized individual Au nanorods. Journal of Materials Chemistry C, 3, 8865–8872.

Scott, R.J., Meffre, S., Woodhead, J., Gilbert, S.E., Berry, R.F., and Emsbo, P. (2009) Development of framboidal pyrite during diagenesis, low-grade regional metamorphism, and hydrothermal alteration. Economic Geology, 104, 1143–1168.

Shannon, R.D. (1976) Revised effective ionic radii and systematic studies of interatomic distances in halides and chalcogenides. Acta Crystallographica, A32, 751–767.

Simon, G., Huang, H., Penner-Hahn, J.E., Kesler, S.E., and Kao, L.-S. (1999) Oxidation state of gold and arsenic in gold-bearing arsenian pyrite. American Mineralogist, 84, 1071–1079.

Steadman, J.A., Large, R.R., Meffre, S., Olin, P.H., Danyushevsky, L.V., Gregory, D.D., Belousov, I., Louneyeva, E., Ireland, T.R., and Holden, P. (2015) Synsedimentary to early diagenetic gold in black shale-hosted pyrite nodules at the Golden Mile deposit, Kalgoorlie, Western Australia. Economic Geology, 110, 1157–1191.

Su, W., Zhang, H., Hu, R., Ge, X., Xia, B., Chen, Y., and Zhu, C. (2012) Mineralogy and geochemistry of gold-bearing arsenian pyrite from Shuiyidong Carlin-type gold deposit, Guizhou, China: Implications for gold depositional processes. Mineralium Deposita, 47, 653–662.

Sunagawa, I., and Takahashi, K. (1955) Preliminary report on the relation between o(111) face of pyrite crystals and its minor contents of arsenic. Geological Society of Japan Bulletin, 6, 1–10.

Sung, Y.-H., Brugger, J., Ciobanu, C.L., Pring, A., Skinner, W., and Nugus, M. (2009) nvisible gold in pyrite and arsenopyrite from multistage Archean gold deposits: Sunrise Dam Eastern Goldfields Province. Mineralium Deposita, 44, 765–791.

Thomas, H.V., Large, R.R., Bull, S.W., Masslennikov, V., Berry, R.F., Fraser, R., Froud, S., and Moye, R. (2011) Pyrite and pyrrhotite textures and composition in sediments, laminated quartz veins, and reefs at Bendigo gold mine, Australia: Insights for ore genesis. Economic Geology, 106, 1–31.

Tomkins, A.G., Pattison, D.R.M., and Frost, B.R. (2007) On the initiation of the metamorphic sulfide anatexis. Journal of Petrology, 48, 511–535.

Wang, C., Chen, Y., Pan, J., Zhang, P., Qi, J., Liu, J., Li, X., and Wang, J. (2010) Speciation analysis of metals (Tl, Cd and Pb) in Tl-containing pyrite and its cinder from Yunfu Mine, China, by La-ICP-MS with sequential extraction. Chinese Journal of Geochemistry, 29, 113–119.

Wood, B.L., and Large, R.R. (2007) Syngenetic gold in western Victoria: Occurrence, age and dimensions. Australian Journal of Earth Science, 54, 711–732.

Yang, J., and Ying, J.Y. (2010) Diffusion of gold from the inner core to the surface of Ag2S nanocrystals. Journal of American Chemical Society, 132, 2114–2115.

Yudovskaya, M.A., Distler, V.V., Chaplygin, I.V., Mokhov, A.V., Trubkin, N.V., and Gorbacheva, S.A. (2006) Gaseous transport and deposition of gold in magmatic fluid: Evidence from the active Kydryavy volcano, Kurile Islands. Mineralium Deposita, 40, 828–848.

Zelenski, M., and Bortnikova, S. (2005) Sublimate speciation at Mutnovsky volcano, Kamchatka. European Journal of Mineralogy, 17, 107–118.

Zhang, J.Y., Ren, D., Zheng, C.G., Zeng, R.S., Chou, C.L., and Liu, J. (2002) Trace element abundances in major minerals of Late Permian coals from southwestern Guizhou province, China. International Journal of Coal Geology, 53, 55–64.

Zhou, T.F., Fan, Y., Yuan, F., Wu, M.A., Hou, M.J., Voicu, G., Hu, Q.H., Zhang, Q.M., and Yue, S.C. (2005) A preliminary geological and geochemical study of the Xiangquan thallium deposit, eastern China: The world's first thallium-only mine. Mineralogy and Petrology, 85, 243–251.

Zhou, T., Fan, Y., Yuan, F., Cooke, D., Zhang, X., and Li, L. (2008) A preliminary investigation and evaluation of the thallium environmental impacts of the unmined Xiangquan thallium-only deposit in Hexian, China. Environmental Geology, 54, 131–145.

Table 1 List of the discussed deposits

Reference	Type of ore deposit	Hg	Tl	Cd	Locality, Mineral Assemblage (MA), Inclusions (INCL)	Analytical methods
Scott et al. (2009)	Sedimentary	–	X	–	Fosterville (Victoria, Australia); MA: py, gn, INCL: N/D	LA-ICP-MS
Hofmann et al. (2009)			X		Belingwe Greenstone Belt (Zimbabwe); South Africa; MA and INCL - N/D	HR-ICP-MS
Berner et al. (2013)		–	X	X	Posidonia Shale (Germany); MA: N/D; INCL: - sph	ICP-MS
Ingham et al. (2014)		–	X	–	roll-front Beverly North uranium deposits (South Australia); MA: py, sph, Se; INCL: Se,	LA-ICP-MS
Large et al. (2014)		–	X	X	Black shale (numerous localities); MA and INCL: N/D	LA-ICP-MS
Marin-Carbonne et al. (2014)		X	X	–	Carbonaceous shales, Bubi Greenstone Belt (Zimbabwe); MA: N/D; INCL: cpy	EMPA, LA-ICP-MS
Palenova et al. (2015)		X	X	X	Kopylovsky and Kavkaz (black shale) (Russia); MA: py, Au, po, cpy, gn, sph,mar, pn, vio, mil, gers, ulm, cob, asp, mo; INCL: Au, cpy, po, gn,	EMPA, LA-ICP-MS
Steadman et al. (2015)		–	X	–	Golden Mile (black shales) (Australia); MA: py, cpy, cas, sph, po, asp, ulm; INCL: sph, cpy, ten, Au, Au-tellurides	LA-ICP-MS
Zhang et al. (2002)	Coal	X	X	–	SW Guizhou province (China); MA and INCL: N/D	ICP-MS
Ding et al. (2001)		X	–	–	SW Guizhou Province (China); MA: py, asp, rlg: INCL: N/D	EMPA, INAA
Zhou et al. (2008)		–	X	–	Xiangquan (Hexian, China); MA: N/D; INCL: Tl-bearing grains	ICP-MS
Hower et al. (2008)		X	X	–	Manchester coal bed, Clay County, (Kentucky, USA); MA: py, mar, claus; INCL:	Micro-PIXE
Cline (2001)	Carlin-type	X	X	–	Getchell, Nevada (USA); MA: py, cpy, asp, gn, sph, mar, stb, rlg; INCL: N/D	EMPA, SIMS
Emsbo et al. (2003)		X	X	–	Meikle, (USA); MA: Au, py, (As,Au)-py, mc, asp, tetr, sph, stb, HgTe, AgTe; INCL: N/D	EMPA, SIMS
Reich et al. (2005)		X	–	–	Deep Star, (Nevada, USA); MA and INCL: N/D	EMPA, SIMS
Su et al. (2012)		X	–	–	Shuiyindong, (Guiuzhou, China); MA: py, asp, mar, orp, rlg, stb; INCL: asp, Au,	EMPA
Barker et al. (2009)		X	X	–	West Banshee, Turquoise Ridge, (Nevada, USA); MA: py, asp, orp, rea; INCL: N/D	EMPA, SIMS
Deditius et al. (2011)		X	–	–	Deep Star (Nevada, USA); MA: N/D; INCL: (Ag,Pb)-sulfides, Au, Ag, Screamer (Nevada, USA); MA: N/D; INCL: cin Lone Tree (Nevada, USA): MA: N/D; INCL: (Au,Ag,As,Ni)-sulphide, (Fe,As,Ag,Ni)-sulphide, (Fe,As,Sb,Pb,Ni,Au)-sulphide	EMPA, SIMS
Large et al. (2009)		–	X	–	Rodeo, Meikle, Gold Quarry (Nevada, USA); MA: py, marc; INCL - N/D	LA-ICP-MS
Scott et al. (2009)		–	X	–	Goldstrike, Gold Quarry, (Nevada, USA); MA: py, mar; INCL: N/D	LA-ICP-MS
Griffin et al. (1991)	Epithermal	X	X	–	North Arm (Queensland, Australia); MA: py, mar, sph, cpy, Ag, Au, naum, frei, asp; INCL: mar, Au, Ag, cpy, sph, gn, po, mo.	PIXE
Cepedal et al. (2008)		X	–	–	El Valle (Spain); MA: py, po, marc, asp, tetr, and, gud, cpy, cov, gn, sph, gr; INCL: asp,	EMPA
Reich et al. (2005)		X	–	–	Porgera (Papua New Guinea); MA and INCL: N/D	EMPA, SIMS
Okrusch et al. (2007)		X	–	–	Wilhelmine mine, (Bavaria, Germany); MA: py, enarg, ten, cpy, bor, dig, dju; INCL: N/D	EMPA
Deditius et al. (2011)		X	–	–	Pueblo Viejo (Dominican Republic); MA: py, enar; INCL: (Pb,Bi,Sb,Ag,Te)-sulphide; Au, Ag, Au-telluride; Ag-Sb. Porgera (Papua New Guinea); MA: N/D; INCL: gn, (Pb,Ag,Sb)-sulphides	EMPA, SIMS
Scher et al. (2013)		X	X	X	Kawah Ijen volcano, Java (Indonesia); MA: N/D; INCL: mo, bis, gn, sph.	LA-ICP-MS
Franchini et al. (2015)		X	–	X	Agua Rica Cu (Mo-Au) (Argentina) (high-sulfidation epithermal part); MA: py, mo, mar, sph, en, kur, cv; INCL: cpy, bn, po,	LA-ICP-MS
Kozmanov et al. (2010)	Porphyry	–	X	–	High-sulphidation epithermal veins overprinting porphyry Cu, Rosia Poieni (Romania); MA-py,en, mo, col, Au-Ag-Bi tellurides, ten, cpy, bn, dig, cov, Te; INCL: cpy, en, bn, cov, Ag-Au tellurides or selenides.	EMPA, LA-ICP-MS

Reference	Type of ore deposit	Hg	Tl	Cd	Locality, Mineral Assemblage (MA), Inclusions (INCL)	Analytical methods
Pass et al. (2010)		X	X	X	Mt. Polley, (British Columbia, Canada); MA: py, cpy, bor; INCL: cpy, gn, sph, Au, telluride; Pt-,Pd-bearing minerals	LA-ICP-MS
Large et al. (2007)	Orogenic gold	–	X	–	Sukhoi Log (Russia); MA: py, asp, po, Au, Au-tellurides; INCL: Au, asp, po, sph, cpy, gn	LA-ICP-MS
Large et al. (2009)					Bendigo (Australia); MA: N/D; INCL: cpy, gn Sukhoi Log (Russia); MA: N/D; INCL: sph, cpy, po, gn, Au Spanish Mt. (Canada); MA: N/D; INCL: cpy, sph, gn	LA-ICP-MS
Wood and Large (2007)		–	X	–	Western Victoria (Australia) – localities in Table 2 therein; MA and INCL: N/D	LA-ICP-MS
Large et al. (2009)		–	X	–	Spanish Mt., (Canada); MA-N/D; INCL: Au, sph, gn, cpy; Sukhoi Log, (Russia); MA: N/D; INCL: Au, sph, cpy, gn, po; Bendigo, (Australia); MA-N/D; INCL: cpy, gn, Pb-Bi-Au tellurides	LA-ICP-MS
Shackleton et al. (2003)		X	–	–	Golden Mile (Australia); MA: py, asp, po, sph, cpy, cv, Au, Te, precious metals tellurides; INCL: Au, clv, syl, kren, ptz.	EMPA
Thomas et al. (2011)		–	X	–	Bendigo, (Australia); MA: py, Au, sph, asp, po, gn; INCL: gn	LA-ICP-MS
Deol et al. (2012)		–	X	–	Bhukja-Jagpura (India); MA: py, asp, po, cpy; INCL: Au,	EMPA, LA-ICP-MS
Cabral et al. (2013)		X	–	X	Antônio Pareira (Brazil); MA: py, asp, po; INCL: N/D	LA-ICP-MS
Li et al. (2014)		–	X	–	Getiaowan-Anba gold deposits, Yangshan gold belt (China); MA: py, MA and INCL: asp, Au, stb, sph, gn, cpy, ten, jam, boul, fam	EMPA, LA-ICP-MS
Duchesne et al. (1983)	Pb-Zn	–	X	–	Pb-Zn deposits (Belgium); MA: py, mar; INCL: hut	SIMS
Revan et al. (2014)	VMS	–	X	X	Pontide orogenic belt (Turkey); MA: py, cpy, sph, gn, bn, Au, Ag, ma, cc, cv, en, Bi, tet, dgn, gersd, INCL: (Au,Ag)-tellurides	LA-ICP-MS
Genna and Gaboury (2015)		–	X	X	Bracemac-McLeod (Canada); MA: py, cpy,gn, sph, INCL: cpy, gn, sph, Ag-Au-Te,	LA-ICP-MS
Agangi et al. (2013)	Witwatersrand	X	–	–	INCL: cpy, gn, Au, sph, po, Au-Ag-Hg alloy,	EMPA, LA-ICP-MS
Yudovskaya et al. (2006)	Volcanic precipitates	–	–	X	Kudryavy volcano (Kurile Islands; Russia); MA: py, gn, sph, cov, cpy, cc, $Pb_4Bi_6S_{13}$, TlCl; INCL: N/D	INAA
Zelenski and Bortnikova (2005)		X	X	X	Mutnovsky volcano, Kamchatka (Russia); MA: py, po, gn, gr, Cd-sulfosalts, TlI; INCL: N/D	EMPA
Biagioni et al. (2013)	Metamorphic	X	X	–	Alpi Apuane (Italy); MA: py, cinnabar, realgar, sph, stb, twinnite, polhemusite, Tl-Hg-As-Sb-Ag-Pb sulfosalts;	EMPA, ICP-MS

Notes: MA = Mineral assemblage, the information is limited to minerals that might contaminate pyrite with Hg, Tl, and Cd. INCL = inclusions in pyrite; N/D = no data. Mineral abbreviations: and = andorite, ani = anilite, asp = arsenopyrite, bis = bismuthinite, bn = bornite, boul = boulangerite, cas = cassiterite, cc = chalcocite, cal = calaverite, cob = cobaltite, clau = clausthalite, cv = covellite, col = colusite, cpy = chalcopyrite, dig = digenite, dju = djurleite, en = enargite, fam = famatinite, frei = freibergite, gersd = gersdorfite, gn = galena, gr = greenockite, gud = gudmundite, hut = hutchinsonite, ida = idaite, jam = jamesonite, kren = krennerite, kur = kuramite, mar = marcasite, mil = millerite, mo = molybdenite, naum = naumannite, orp = orpiment, pn = pentlandite, po = pyrrhotite, py = pyrite, ptz = petzite, rlg = realgar, sph = sphalerite, spi = spinkopite, stb = stibnite, ten = tennantite, tetr = tetrahedrite, ulm = ulmanite, vio = violarite, yar = yarrovite.

Figure 1 Concentrations of Hg, Tl, and Cd as a function of As concentration in pyrite (in parts per million; log-log scale). Gray dashed line depicts the solubility limit of Au in pyrite as a function of As content after Reich et al. (2005). Distribution of the analyses in metal-As log-log space as a function of the type of ore deposit. (**a**) Solubility limit of Hg in arsenian pyrite compared to the solubility of Au in arsenian pyrite. (**b**) Solubility limit of Tl in arsenian pyrite compared to the solubility of Au in arsenian pyrite. (**c**) Concentration of Cd vs. As in arsenian pyrite compared to the solubility of Au in arsenian pyrite. Note the thick, black, dashed line outlining the data points that represent Cd-rich sphalerite inclusions in pyrite from VMS deposits and hydrothermal vents. The summary of literature data is provided in Table 1.
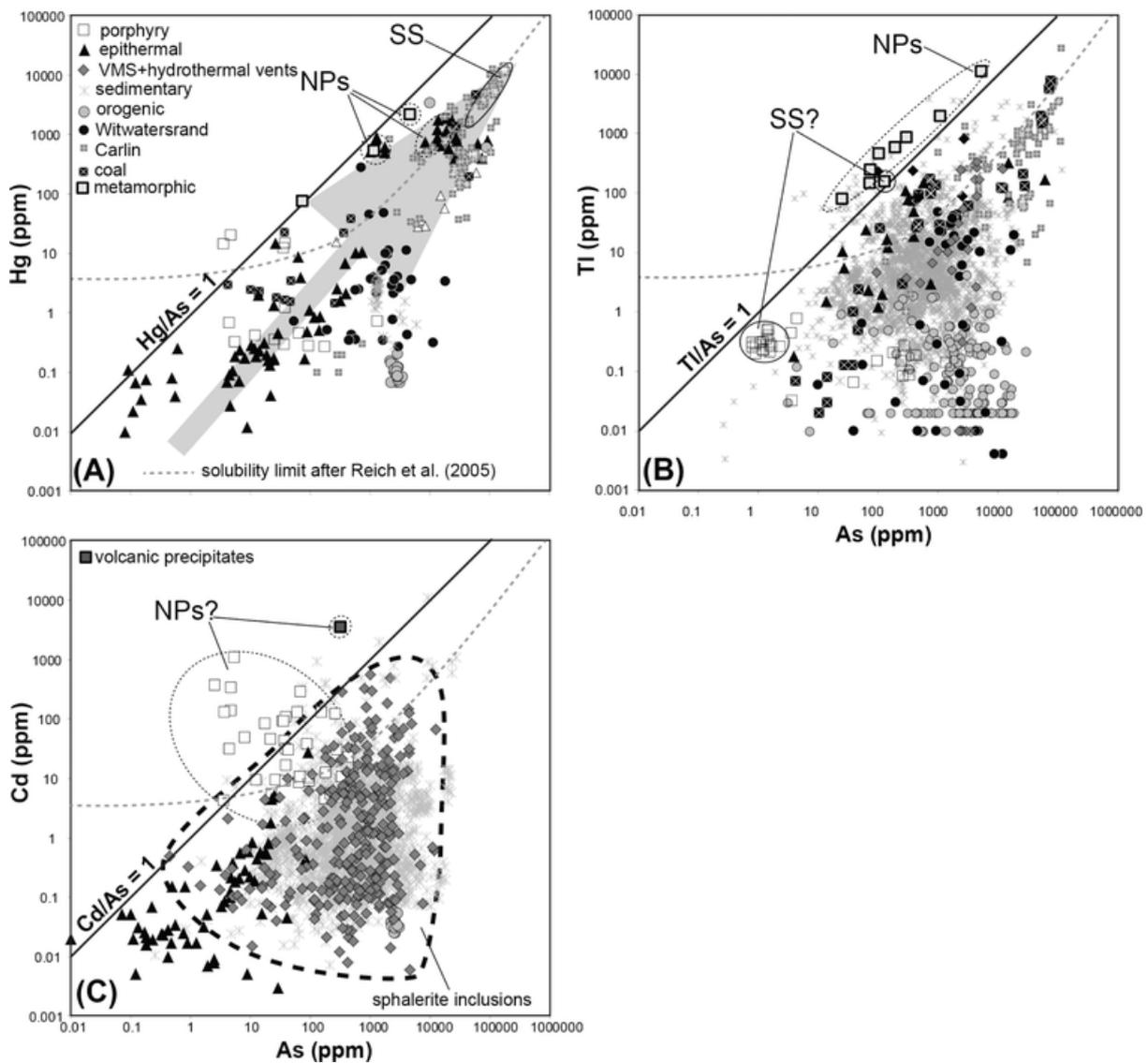
Figure 2 Solubility of metals (Au, Hg, Tl) in arsenian pyrite in As-metal-T (log-log-°C) space. Note the shift of the solubility limit along the solubility surface as a function of changing temperature.